Supplementary Information

Pore-Scale Salt Precipitation and Transport in Fractures during Carbon Dioxide Storage: Roles of Fracture Geometry, Brine Chemistry, and Phase State

Shanchao Liu[a], Zengding Wang[a], Kaiyue Ding[a], Yulin Zhang[a], Chuang Ning[a], Cunqi Jia[b], Mingshan Zhang[c], Jun Yao[a], Hai Sun[a], Yongfei Yang[a], Lei Zhang[a], Junjie Zhong[a]*

[a] *State Key Laboratory of Deep Oil and Gas, China university of Petroleum (East China), Qingdao 266580, P.R. China*

b Hildebrand Department of Petroleum and Geosystems Engineering, The University of Texas at Austin, Austin, Texas, USA

c School of Vehicle and Energy, Yanshan University, Qinhuangdao, China, 066000

*Corresponding authors. Email address: zhongjunjie@upc.edu.cn (J.Z.)

List of captions

Section 1: Microfluidic Chip Design and Configuration

Three microfluidic models—unfractured, discrete fracture, and interconnected fracture—were designed based on the geological parameters in Table S1 (Fig. S1a). Model geometries are summarized in Table S2.

Table S1. Geological parameters from representative geological carbon storage (GCS) projects

Project	Lithology	Region	Porosity	Pore Size Range
Sleipner (North Sea, Norway)[1]	Utsira	Reservoir	30-35%	10–100 μm
	Nordland Shale	Caprock	<10%	<1 μm
Paris Basin (France)	Dogger Limestone[2]	Reservoir	14.5%	1–10 μm
	Callovo-Oxfordian Shale[3]	Caprock	6%	5–100 nm
Jianghan Basin (China)[4]	Xingouzui Sandstone	Reservoir	17%	10–100 μm
	Mudstone	Caprock	7.5%	<1 μm
Generic Shale reservoir	Shale	Matrix[5]	3.0–4.8%	Nanopores
	/	Fractures[6, 7]	1–10%	/

Table S2. Design parameters of microfluidic chip models used in this study

Fracture structure	Reservoir region porosity (%)	Caprock region porosity (%)	Fracture region porosity (%)
Unfractured model	14.86	1.71	/

Discrete fracture model	14.86	1.71	3.26
Interconnected fracture model	13.80	1.71	10.89

The microfluidic chips used in experiments consist of three functional domains: the reservoir region, the caprock region, and the fracture region. The reservoir region is composed of randomly packed circular obstacles with diameters of 80, 150, and 500 μm, forming a heterogeneous pore structure with channel widths of 10, 40, 60, 100, and 150 μm. This region is etched to a depth of 10 μm (Fig. S1b). The caprock region features a regular array of square cells (1000 μm side length) connected by 10 μm-wide channels, with a total etching depth of 1 μm (Fig. S1c). The fracture region comprises open channels with widths of 40, 60, 100, and 150 μm, etched to a depth of 40 μm to simulate conductive fracture pathways (Fig. S1d).

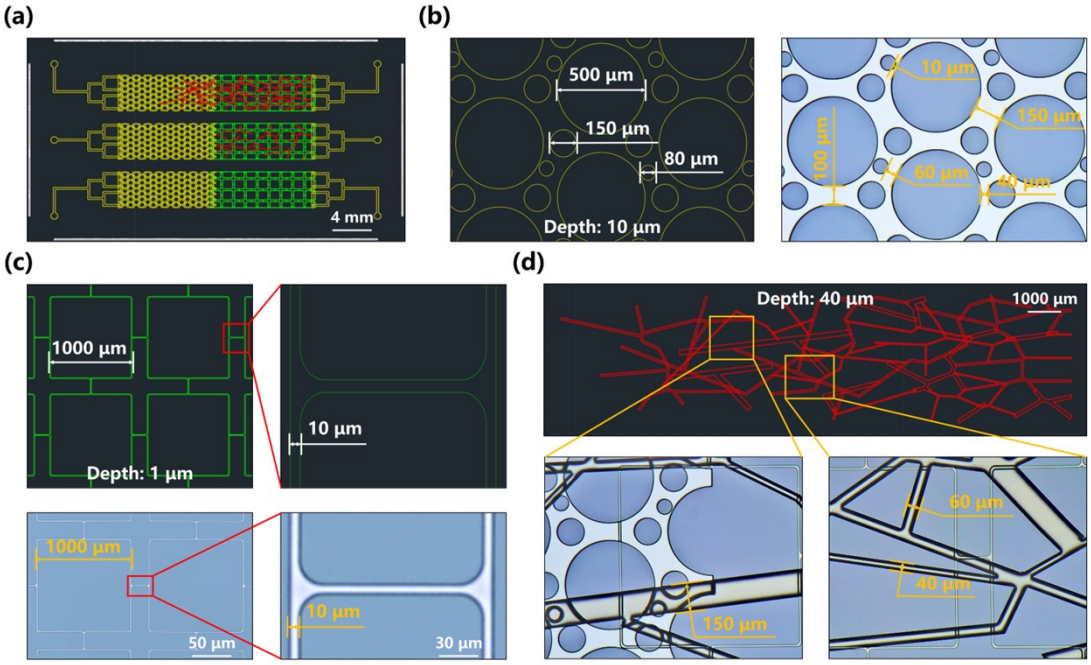

Fig. S1. Design and visualization of microfluidic chip models: (a) full chip layout; (b) reservoir region; (c) caprock region; (d) fracture region.

Section 2: Experimental Cases and Procedures

Table S3 summarizes 18 experimental cases. Microfluidic experiments investigated the effects of fracture geometry, CO_2 phase, and brine composition on salt precipitation, aggregation, and migration. The chip included unfractured, discrete fracture, and interconnected fracture models to simulate caprock–reservoir fracture conditions. Displacement conditions included gas-phase CO_2 (5.5 MPa, 60 °C) and supercritical CO_2 (8.5 MPa, 60 °C). Brine compositions consisted of 20 wt% NaCl, 20 wt% $CaCl_2$, and a mixed solution with 10 wt% of each salt.

Table S3. Details of Experimental Cases.

Case	Fracture structure	CO_2 phase	Brine composition
1	Unfractured model	Gas	20wt% NaCl
2			20wt% $CaCl_2$
3			10wt% NaCl+10wt% $CaCl_2$
4		Supercritical	20wt% NaCl
5			20wt% $CaCl_2$
6			10wt% NaCl+10wt% $CaCl_2$
7	Discrete fracture model	Gas	20wt% NaCl
8			20wt% $CaCl_2$
9			10wt% NaCl+10wt% $CaCl_2$
10		Supercritical	20wt% NaCl
11			20wt% $CaCl_2$
12			10wt% NaCl+10wt% $CaCl_2$
13	Interconnected fracture model	Gas	20wt% NaCl
14			20wt% $CaCl_2$
15			10wt% NaCl+10wt% $CaCl_2$

16		20wt% NaCl
17	Supercritical	20wt% $CaCl_2$
18		10wt% NaCl+10wt% $CaCl_2$

The experimental setup was designed to observe salt precipitation and migration during CO_2 leakage (Fig. 1b). The setup includes a chip manifold, injection system, temperature control unit, monitoring system, imaging system, and vacuum line. The chip manifold is made of C-276 Hastelloy, which resists corrosion and operates at up to 100 °C and 30 MPa. The injection system consists of a 60 MPa pressure-rated reservoir and a high-precision pump (XHC-D, 0.01 MPa resolution). A thermostatic water bath circulates deionized water to maintain the temperature. Temperature and pressure are monitored with a multi-channel thermometer (UNI-T UT3208) and a precision pressure sensor (OMEGA PX409). Five thermocouple ports are evenly distributed within the chip holder for accurate temperature feedback. The imaging system uses an Axio Scope.A1 microscope with 4× and 10× objectives and a CMOS camera (5440 × 3648 pixels, 15 Hz).

A novel experimental method was developed to dynamically visualize salt precipitation process resulting from CO_2–brine interactions under pore-scale conditions. This method enables precise simulation of reservoir pressure and temperature, facilitating in-situ observation of the nucleation, growth, and migration of salt crystals during CO_2 injection. By combining microfluidic control, real-time imaging, and quantitative data analysis, the system captures the temporal evolution of

salt morphology and its effects on pore structure, permeability, and fracture sealing under different chip geometries and CO_2 phase states.

Experimental procedures and parameters.

Step 1: Assemble microfluidic apparatus. A clean microfluidic chip is installed into the manifold, and nitrile O-rings are used to seal inlet and outlet ports to prevent leakage.

Step 2: Calibrate the optical imaging system. The microscope is adjusted to ensure accurate and sharp focus. Camera settings such as flat-field correction, contrast, brightness, and saturation are optimized to ensure image clarity and distinguishability across different flow channel regions.

Step 3: Introduce a small amount of CO_2 at atmospheric pressure to displace residual air in chip and tubing. Leak tightness is checked, and then vacuum pump is activated to evacuate system for 4 hours until internal pressure drops below 10 Pa.

Step 4: Activate thermostatic water bath and set temperature to 60 °C. After at least 30 minutes of heating, the internal temperature at multiple points in chip is verified via thermocouples inserted into manifold ports to ensure thermal equilibrium.

Step 5: Saturate chip with brine. The dual-cylinder pump at brine inlet is set to constant pressure mode at P_1 = 0.5 MPa to drive at least 100 pore volumes brine from an intermediate reservoir and fully saturate microfluidic network.

Step 6: Pressurize chip to simulate subsurface conditions. The CO_2-side dual-cylinder pump is also set to constant pressure mode at $P_2 > P_1$. The pressure differential

(P_2 - P_1) is optimized to enable controlled advancement of CO_2-brine interface. Once P_2 reaches target pressure, both P_1 and P_2 are equilibrated to maintain stable system pressure. In our experiments, a pressure differential of 0.1 MPa was applied, which represents the minimum driving pressure required for stable displacement of CO_2-brine interface in unfractured model.

Step 7: Record experimental data. During the initial two hours, full-chip images are acquired every 10 minutes. In the subsequent two hours, images are taken every 15 minutes. This imaging protocol captures the dynamic evolution of brine evaporation, salt nucleation, crystal aggregation, and transport within the chip.

Under storage-relevant conditions, representative dynamic viscosities are $\mu_{gas\text{-}phaseCO2} \approx 1\text{-}2\times10^{-5}$ Pa·s, $\mu_{scCO2} \approx 2\text{-}4\times10^{-5}$ Pa·s, while CO_2 solubility in 1-3 wt% NaCl brines at 30-60 °C and 10-20 MPa is on the order of 10^{-2} in mole fraction[8, 9]. Under our conditions, μ_{scCO2} is only a few times larger than $\mu_{gas\text{-}phaseCO2}$ but ~20-50 times smaller than μ_{brine}, so both CO_2 states remain much less viscous than brine[8, 10]. This supports the interpretation that differences in salt coverage mainly arise from film connectivity and evaporation capacity rather than from large changes in average S_{wr}.

Table S4 presents the water saturation values for all cases after CO_2 breakthrough.

Table S4. Water Saturation in Different Chip Geometries.

Case	Water saturation after CO_2 breakthrough (%)		
	Reservoir zone	Caprock zone	Fracture zone
1	30.48	0	/
2	30.93	0	/

3	28.74	0	/
4	38.52	0	/
5	40.03	0	/
6	37.39	0.67	/
7	31.04	33.96	3.31
8	32.03	31.99	3.45
9	31.98	31.87	3.33
10	39.30	40.35	5.44
11	44.46	44.90	5.68
12	42.55	40.12	4.78
13	33.53	21.67	16.30
14	34.08	19.87	22.22
15	33.09	22.68	18.69
16	41.79	30.31	36.46
17	43.41	35.79	35.98
18	39.67	39.86	38.29

Section 3: Salt Coverage Distribution in Unfractured Model

Salt precipitation in unfractured model primarily occurred within reservoir region (Fig. S2). Taking NaCl brine as an example, more than 97% of salt coverage induced by gas-phase CO_2 displacement accumulated in reservoir region (Fig. S2c), while caprock region primarily served as a migration pathway for nanoscale salt particles (Fig. S2a). More than 99% of salt coverage induced by $scCO_2$ displacement accumulated in reservoir region (Fig S2d), and the caprock region again functioning mainly as a conduit for particle transport (Fig. S2b). Therefore, in unfractured model, our analysis focuses on salt precipitation dynamics occurring within reservoir region.

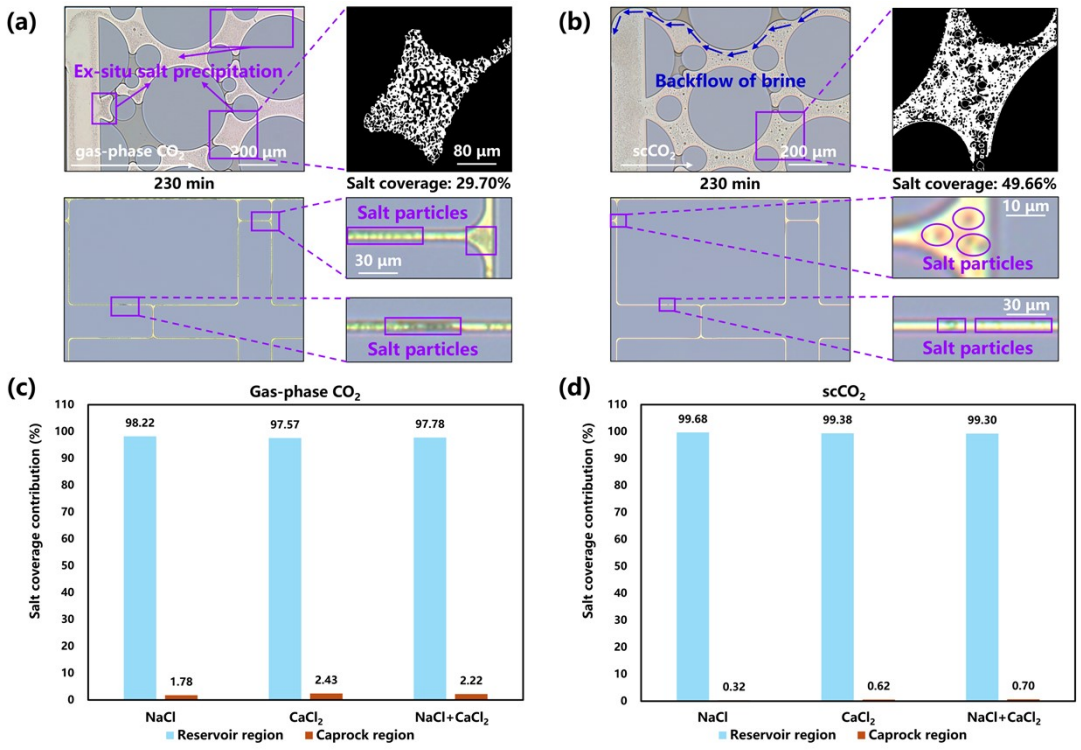

Fig. S2. Visualization of salt precipitation in different regions under gas-phase CO_2 (a) and supercritical CO_2 (b) displacement of NaCl brine. Comparison of salt coverage contribution from reservoir and caprock regions for different brine compositions under (c) gas-phase CO_2 and (d) supercritical CO_2 conditions.

Section 4: Salt Migration Traces at the Outlet in Unfractured and Discrete Fracture Model

The unfractured model experiments demonstrated that both CO_2 phase and brine composition significantly influence salt precipitation (Fig. S3). Compared with gas-phase CO_2, $scCO_2$ resulted in higher salt coverage due to its higher viscosity and brine evaporation flux.

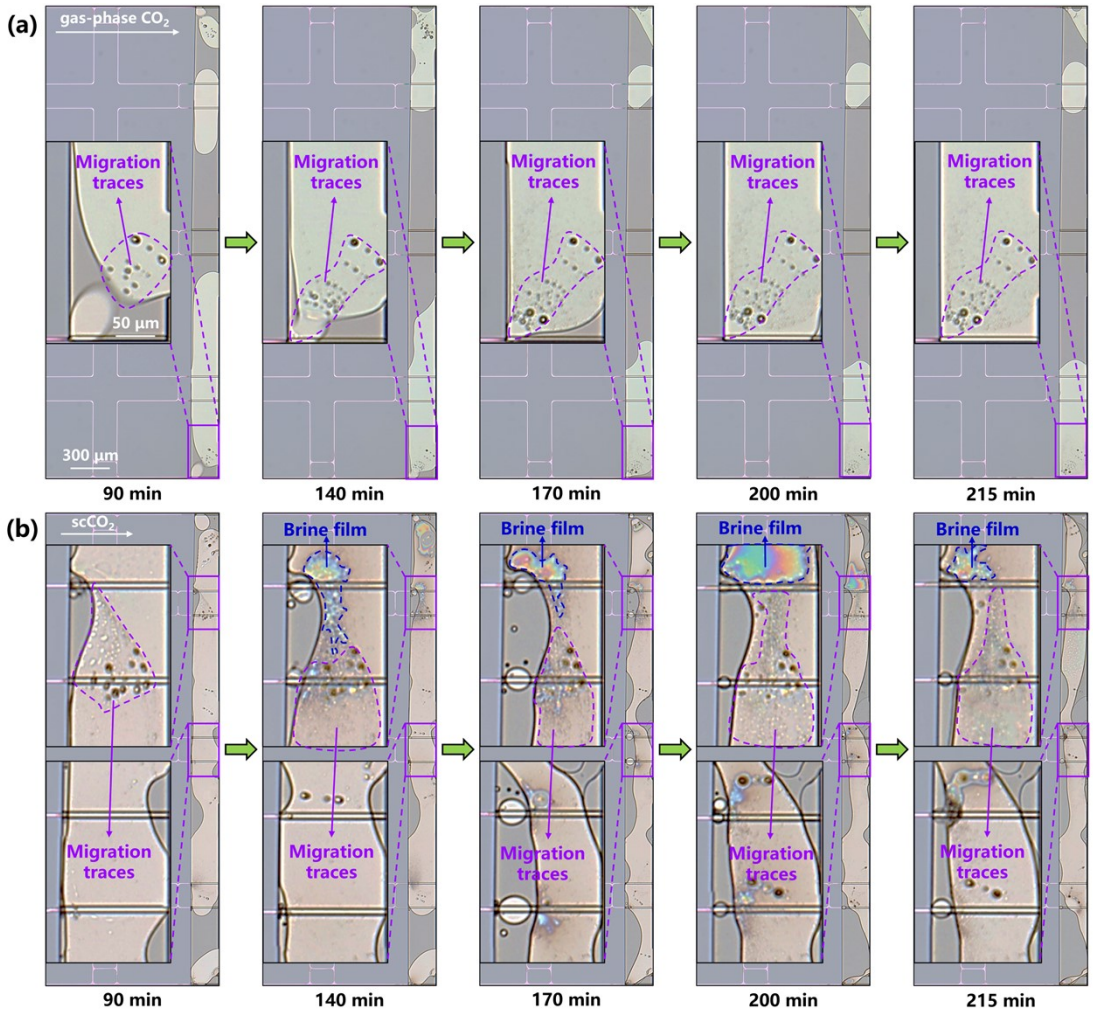

Fig. S3. Visualization of salt particle migration traces in different regions of unfractured model under different phases CO_2 displacement using NaCl brine. (a) gas-phase CO_2. (c) $scCO_2$.

The discrete fracture model shows significantly higher salt coverage, as fractures provide more space for accumulation. In fractures, salt precipitation is driven by salt aggregation and migration. Taking NaCl brine as an example, salt aggregates formed under gas-phase CO_2 displacement exhibited loose structures and were prone to salt particle migration (Fig. S4). In contrast, under supercritical CO_2 displacement, the salt aggregates formed were structurally compact and more stable, exhibiting limited particle mobility (Fig S5).

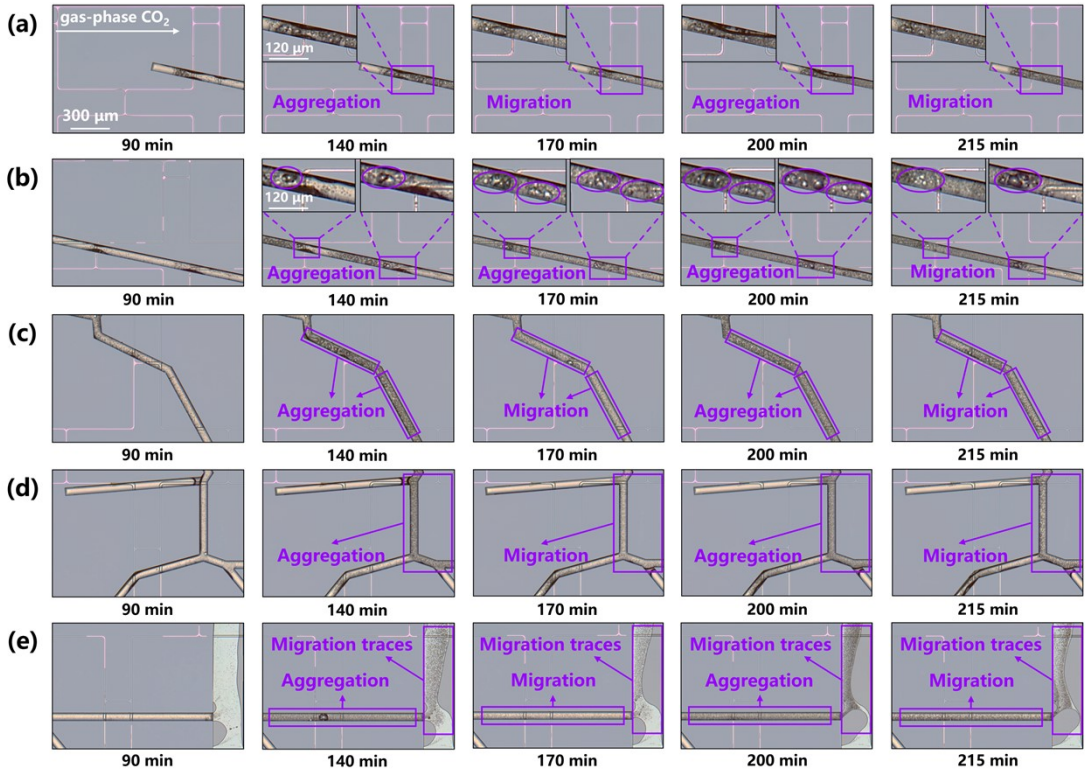

Fig. S4. Visualization of salt particle migration in different regions of discrete fracture model under gas-phase CO_2 displacement using NaCl brine. (a) Region 11, (b) Region 12, (c) Region 27, (d) Region 41, (e) Region 42.

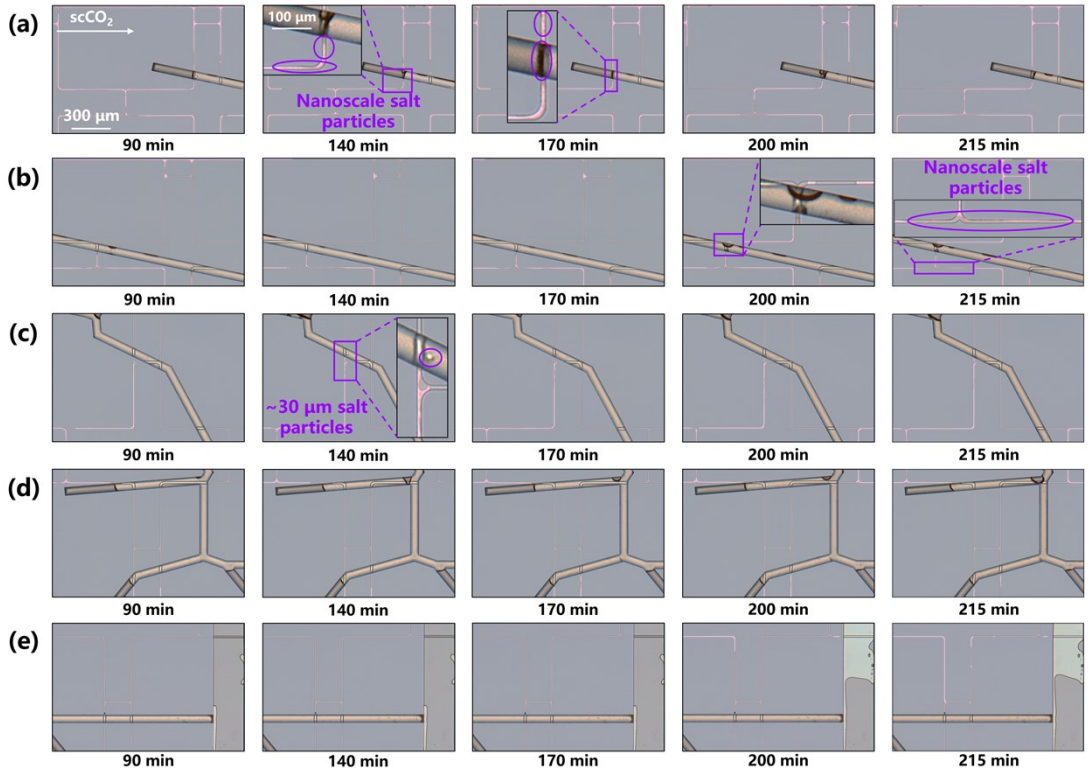

Fig. S5. Visualization of salt distribution in discrete fracture model under supercritical CO_2 displacement using NaCl brine. (a) Region 11, (b) Region 12, (c) Region 27, (d) Region 41, (e) Region 42.

Section 5: Salt Coverage Evolution in Discrete Fracture Model

In discrete fracture model, the aggregation and migration of salt particles within fracture region significantly influenced overall salt coverage, resulting in noticeable fluctuations in temporal coverage curves (Fig. S6).

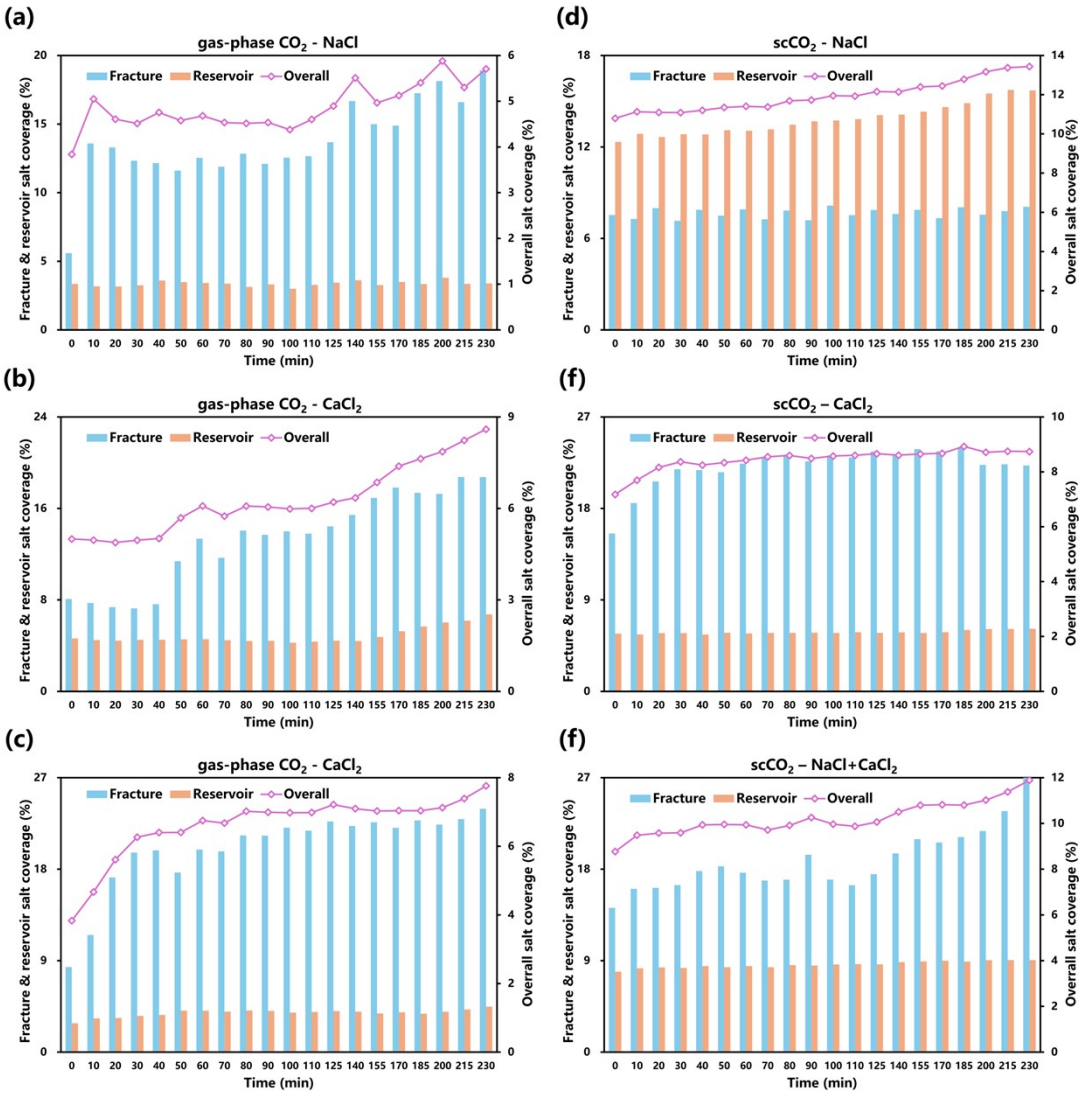

Fig. S6. Comparative analysis of salt coverage evolution in reservoir region, fracture region, and entire domain in discrete fracture model. (a-c) Gas-phase CO_2 injection under different brine compositions, (d-f) Supercritical CO_2 injection under different brine compositions.

Section 6: Brine Film Formation within Fractures in Interconnected Fracture Model

Salt precipitation at the reservoir-fracture joint in interconnected fracture model progresses through three stages during gas-phase CO_2 injection (Fig. S7).

Stage I: Gas-phase CO_2 rapidly displaces brine from reservoir and breaks through fracture network. Owing to low viscosity and high mobility, CO_2 bypasses residual brine and forms discrete, locally distributed brine films along the hydrophilic fracture walls. These capillary-stabilized films serve as initial sites for salt precipitation.

Stage II: Continued CO_2 injection leads to evaporation of brine films, increasing local salinity and triggering salt precipitation. High fracture connectivity enables migration of micron-sized salt particles (~10 μm) with CO_2 flow, while nanoscale particles adhere to fracture surfaces. The patchy brine film distribution results in uneven salt coverage and sporadic particle transport.

Stage III: Ongoing evaporation further elevates salinity within residual brine films, creating a concentration gradient that drives brine inflow from adjacent reservoir regions. Replenished brine spreads and evaporates along the channel walls, sustaining salt precipitation both within fracture and near reservoir joint. The intermittent film distribution leads to fragmented salt accumulation and partial particle migration.

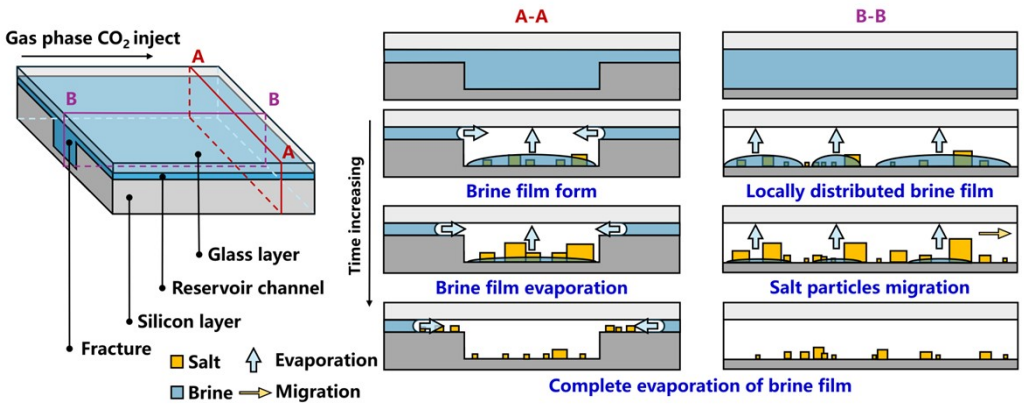

Fig. S7. Schematic illustration of brine film formation, evaporation, salt precipitation, and reaccumulation within microfluidic chip under gas-phase CO_2 displacement.

During supercritical CO_2 ($scCO_2$) injection, salt precipitation at the reservoir–fracture interface evolves through three stages (Fig S8). Compared to gas-phase CO_2, the higher viscosity of $scCO_2$ significantly alters brine film formation and distribution.

Stage I: The slower propagation of $scCO_2$ through reservoir and into fracture facilitates the formation of a continuous brine film along hydrophilic fracture walls. Unlike discontinuous films observed with gas-phase CO_2, this film is spatially stable and uniformly coats fracture surfaces.

Stage II: Continued injection leads to gradual evaporation of brine film and initiates salt precipitation. Micron-sized salt crystals—$CaCl_2$ (~30 μm) and NaCl (~10 μm)—may begin to migrate, but most remain immobilized. This immobilization results from protective brine film surrounding the particles, which suppresses large-scale transport. Only uncoated or partially exposed particles migrate, slowing the net increase in salt coverage.

Stage III: Persistent evaporation near injection point raises local salinity within fracture, creating a gradient that drives brine inflow from adjacent reservoir. The unsaturated brine reaccumulates as a film near injection front and spreads along fracture walls under interfacial tension. This brine film reaccumulation mechanism sustains localized salt precipitation and limits particle migration, resulting in more stable and spatially confined salt coverage.

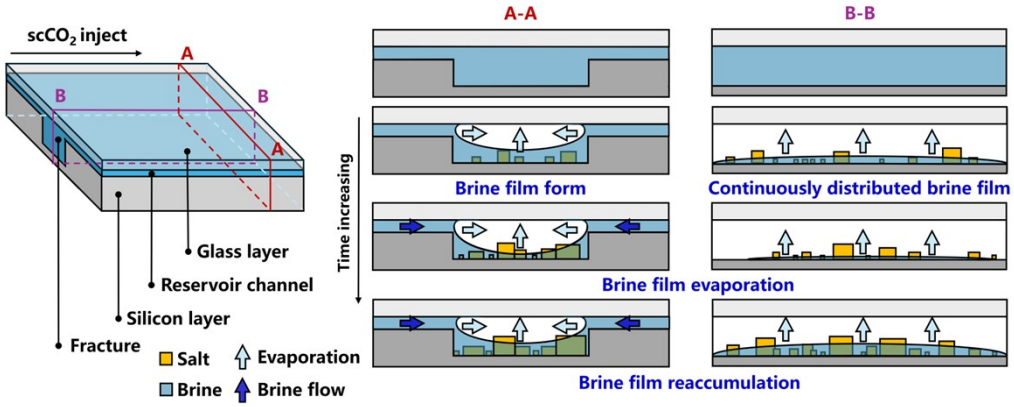

Fig. S8. Schematic illustration of brine film formation, evaporation, salt precipitation, and reaccumulation within microfluidic chip under $scCO_2$ displacement.

References

1. E. Stavropoulou and L. Laloui, *Sci Rep*, 2022, **12**, 10706.
2. B. Brigaud, B. Vincent, C. Durlet, J. F. Deconinck, P. Blanc and A. Trouiller, *Journal of Sedimentary Research*, 2010, **80**, 791-807.
3. O. Bildstein, C. Kervévan, V. Lagneau, P. Delaplace, A. Crédoz, P. Audigane, E. Perfetti, N. Jacquemet and M. Jullien, *Oil & Gas Science and Technology – Revue de l'Institut Français du Pétrole*, 2010, **65**, 485-502.
4. S. Peng, H. Shan, Y. Li, Z. Yang and Z. Zhong, *Procedia Earth and Planetary Science*, 2013, **7**, 669-672.
5. J. Jing, Y. Yang, J. Cheng, X. Jing and Z. Ding, *Energy & Fuels*, 2024, **38**, 11891-11908.

6. C. Zou, D. Dong, S. Wang, J. Li, X. Li, Y. Wang, D. Li and K. Cheng, *Petroleum Exploration and Development*, 2010, **37**, 641-653.
7. K. Larssen, K. Senger and S.-A. Grundvåg, *Marine and Petroleum Geology*, 2020, **122**.
8. S. Bando, F. Takemura, M. Nishio, E. Hihara and M. Akai, *J. Chem. Eng. Data*, 2003, **48**, 576-579.
9. L. Liu, W. Zhu, C. Wei, D. Elsworth and J. Wang, *Journal of Petroleum Science and Engineering*, 2018, **164**, 91-102.
10. N. Spycher and K. Pruess, *Geochimica et Cosmochimica Acta*, 2005, **69**, 3309-3320.